Guiding Stem Cell Tenogenesis by Modulation of Growth Factor Signaling and Cell-Scale Biophysical Cues in Bioengineered Constructs

Simão P. B. Teixeira, Alberto Pardo, Syeda M. Bakht, Manuel Gomez-Florit, Rui L. Reis, Manuela E. Gomes,* and Rui M. A. Domingues*

Tendon injuries and tendinopathies are increasingly prevalent health problems currently lacking effective treatments. Tissue engineering offers promising strategies to boost the low innate regenerative ability of tendons. Within this context, the simultaneous leveraging of both physical and biochemical cues by engineered scaffolding systems can be explored to promote a stronger tenogenic response from stem cells. Here, molecularly imprinted polymeric nanoparticles (MINPs) against transforming growth factor (TGF)-β3 are combined with bioinspired anisotropic hydrogels to produce tenogenesis-inductive constructs. MINPs are first solid phase-imprinted against a TGF-β3 epitope, achieving an affinity comparable to monoclonal antibodies. MINPs and magnetically-responsive microfibers are then encapsulated together with adipose-derived stem cells within gelatin-based hydrogels, applying a magnetostatic field during gelation to align the microfibers. The created anisotropic microstructure guides cell growth and elongation unidirectionally, while MINPs act as artificial receptors for TGF-β3, potentiating its paracrine action in the cellular microenvironment. The combination of both stimuli proves effective at increasing TGF-β signaling, which promotes the expression of tendon-associated genes and corresponding protein synthesis, suggesting that microstructural cues and biomolecule sequestration act in tandem to direct cell fate commitment. Overall, this system recapitulates several elements of tendon development, constituting a promising strategy for the regeneration of this tissue.

1. Introduction

Tendons are dense connective tissues responsible for the transmission of forces between muscle and bone, thus allowing locomotion.[1] Although tendon-associated diseases are often overlooked by the healthcare field, tendinopathy and acute tendon injuries are global health problems affecting millions of people worldwide every year.[2] They account for up to 50% of musculoskeletal-related primary care visits, and these figures are expected to rise due to the aging population and increasing sporadic sports activity, placing a great burden on healthcare systems. This scenario is further exacerbated by the fact that currently available treatments, from physiotherapy to surgery or infiltrations, fail to completely restore tissue functionality, increasing the recurrence of subsequent injuries.[3–5] To improve this outcome, it is essential that the development of new therapies considers both the structure and biological specificities of tendons. The extracellular matrix (ECM) comprises ≈80% of the tendon structure, with collagen type

S. P. B. Teixeira, A. Pardo, S. M. Bakht, M. Gomez-Florit, R. L. Reis,
M. E. Gomes, R. M. A. Domingues
3B's Research Group
I3Bs – Research Institute on Biomaterials
Biodegradables and Biomimetics of University of Minho
Headquarters of the European Institute of Excellence on Tissue
Engineering and Regenerative Medicine
AvePark – Parque de Ciência e Tecnologia, Zona Industrial da Gandra,
Barco GMR 4805-017, Portugal
E-mail: megomes@i3bs.uminho.pt; rui.domingues@i3bs.uminho.pt

The ORCID identification number(s) for the author(s) of this article can be found under https://doi.org/10.1002/adfm.202312961

S. P. B. Teixeira, A. Pardo, S. M. Bakht, M. Gomez-Florit, R. L. Reis,
M. E. Gomes, R. M. A. Domingues
ICVS/3B's–PT Government Associate Laboratory
Braga/Guimarães Portugal

A. Pardo
Colloids and Polymers Physics Group
Particle Physics Department and Materials Institute (iMATUS)
University of Santiago de Compostela
Santiago de Compostela 15782, Spain

M. Gomez-Florit
Health Research Institute of the Balearic Islands (IdISBa)
Palma 07010, Spain

I making up ≈70% of its dry weight.[6] Tendon ECM architecture is organized in a highly hierarchical and anisotropic fibrous structure, aligned according to the load-bearing axis,[8] which is crucial to ensure that tendons can sustain extremely high tensile forces. The scarce resident cell population is mainly composed of tenocytes, tendon-specific fibroblast-like cells, organized in rows between collagen bundles and displaying highly-elongated morphologies along the longitudinal dimension. The hypovascular and hypocellular nature of this tissue contributes to its poor healing response to injury, resulting in the deposition of a fibrotic-like matrix that does not recover the original tissue architecture, which is key for its function.[2]

In this context, tissue engineering and regenerative medicine (TERM) approaches have been increasingly researched in recent years as alternative options for tendon therapies.[7,8] These strategies aim to promote tissue regeneration by carefully designing biomaterials that recapitulate the main cues of tissue development. Exciting progress in the TERM field over the last few decades has led to an increased interest in how different physical cues, like matrix stiffness, geometry or topography, can influence cell behavior.[9–11] Considering the aforementioned characteristics of tendon ECM, biomaterial scaffolds with unidirectional anisotropic patterns have been widely exploited for this purpose.[12–14] Hydrogels have been among the most researched scaffolding materials, owing to their similarity to the natural ECM, as a polymer network with high water content, as well as the ability to easily tune their physical and chemical properties.[15] Nonetheless, creating anisotropic 3D architectures within bulk hydrogels is challenging.[16] Different fabrication techniques have been explored for this purpose, including directional freeze-casting,[17] assembly of microgel units[18] or application of shear or tensile forces.[19] But most of them provide only a limited control over the hydrogel architecture, while also lacking post-processing actuation capabilities.[20] In this sense, the orientation of fiber-like microfillers within the hydrogel bulk has emerged as one of the most successful design approaches in this field.[21] Recently, we have demonstrated that short electrospun magnetically-responsive microfibers (sMRFs) can be oriented within gelatin-based hydrogels to generate anisotropic microstructures that guide cell spatial organization and morphology in three dimensions, thereby overcoming some of the previously identified shortcomings of anisotropic hydrogel design.[20] By further modifying the sMRFs with tendon decellularized (d)ECM and providing remote magneto-mechanical stimulation during in vitro culture period, these constructs could induce the tenogenic commitment of encapsulated stem cells.[20]

Additionally, it has also become increasingly evident that the synergy between structural and soluble cues is essential for an effective recreation of lineage differentiation steps.[22–25] Following this rationale, several recent studies have demonstrated the potential of composite systems capable of simultaneously modulating both types of stimuli by providing a controlled release of specific bioactive molecules like growth factors (GFs).[26–29] However, the use of exogenous biomolecules in these systems also presents several intrinsic limitations, such as their extremely-short half-lives, requiring the use of high doses to obtain relevant biological effects.[30,31] Consequently, the costs associated with such strategies would significantly contribute to increase the financial pressure over healthcare systems, hindering their clinical adoption.

Additionally, the use of such doses could cause adverse immune reactions or untargeted effects.

An alternative approach is the design of biomaterials inspired by the natural ECM that can sequester these molecules as they are endogenously produced by local cells.[30,32] In this manner, affinity-bound GFs are stabilized locally, prolonging and amplifying their action on cell receptors.[33,34] However, traditionally used GF sequestering molecules are either unspecific (e.g., fibronectin, heparin), expensive (antibodies), or require laborious discovery procedures (peptides, aptamers).[30,31] To tackle this challenge, we have previously demonstrated that molecularly imprinted polymeric nanoparticles (MINPs) could act as artificial GF receptors.[32] This drastically reduced or even abolished the need for the administration of exogenous recombinant GFs to promote a specific stem cell fate commitment in vitro. In comparison to previous approaches, MINPs are synthesized from affordable commercially available monomers typically applied on the synthesis of several polymeric biomaterials with approval for clinical uses. Moreover, they can achieve high affinity and selectivity for the target molecule with a greatly reduced development time.[31,35]

Building on these concepts, we hypothesized that the combination of the two previous elements – MINPs for modulation of soluble cues and sMRFs for modulation of biophysical cues – in a single *tenogenic construct* would generate a synergistic effect, leading to a more robust and effective promotion of tenogenesis. To that end, we prepared a new class of MINPs with particularly high affinity for the target molecule by a solid phase imprinting method.[36,37] In parallel, bioinspired composite hydrogels were developed by aligning the incorporated sMRFs through the application of low intensity magnetic fields, thus creating a 3D anisotropic fibrous topography reminiscent of native tendons which modulated the morphology and spatial organization of encapsulated cells. MINPs were integrated in the structure of biomimetic hydrogels to serve as synthetic receptors for transforming growth factor (TGF)-β3, sequestering this pro-tenogenic molecule[38,39] and amplifying its paracrine signaling.[31] To test these concepts, human adipose tissue-derived stem cells (hASCs) were selected for encapsulation in tenogenic constructs, since they are a widely available source of mesenchymal-type stem cells, with the capability of differentiating into the tenogenic lineage.[40,41] We show that the developed systems boosted TGF-β signaling in a MINP concentration- and sMRF alignment-dependent manner, with this being translated into a pro-tenogenic gene expression pattern and corresponding increases in tendon-related proteins. Remarkably, these pro-tenogenic effects were only observed when insoluble and soluble stimuli were concomitant in the cellular microenvironment, confirming the hypothesis of a synergistic interaction between both cues on driving cell fate. **Figure 1** schematically depicts our proposed design strategy and its biological outcomes.

2. Results and Discussion

2.1. Solid Phase Molecularly Imprinted Nanoparticles Bind and Retain TGF-β3 with High Affinity

The first step toward building the proposed tenogenic constructs was the imprinting of polymeric nanoparticles against TGF-β3.

**ADVANCED
SCIENCE NEWS**

www.advancedsciencenews.com

**ADVANCED
FUNCTIONAL
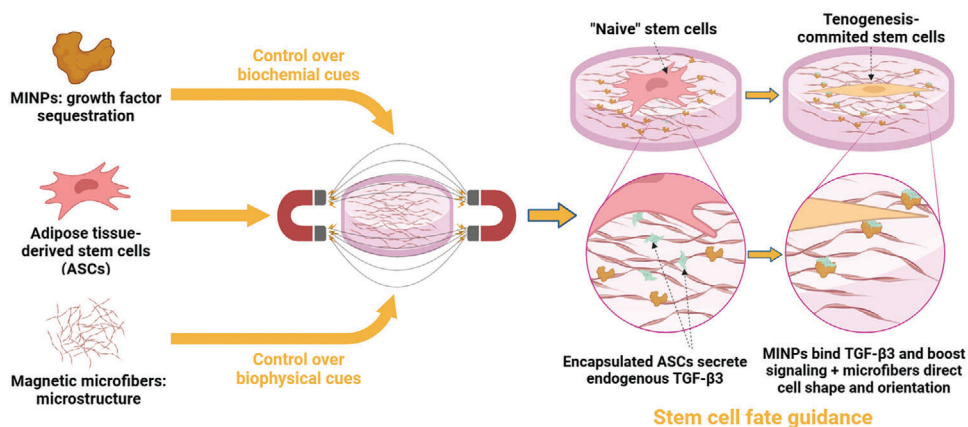MATERIALS**

www.afm-journal.de

Figure 1. Schematic representation of the proposed tissue engineering strategy for the development of tenogenic constructs. In this design, magnetically aligned microfibers are expected to provide an adequate anisotropic microstructure to guide cell spreading directionality and organization through contact guidance. Concomitantly, molecularly imprinted polymeric nanoparticles (MINPs) are sought to sequester transforming growth factor (TGF)-β3 endogenously secreted by human adipose tissue-derived stem/stromal cells (hASCs), thereby prolonging and amplifying its paracrine signaling effects. The combined control over both biochemical and biophysical cues is expected to synergistically drive a more robust tenogenic commitment in encapsulated hASCs.

To obtain a population of MINPs with a homogeneous distribution of affinities for the target protein, we followed the solid phase imprinting method schematically represented in **Figure 2A**.[42,43] A previously tested N-terminal conformational epitope of TGF-β3[31] was used as a template molecule instead of the full protein to minimize production costs while increasing efficiency and reproducibility.[35] Derivatization of the solid phase support (glass microspheres) with the epitope peptide was confirmed by labelling with fluorescein isothiocyanate (FITC) (Figure 2B; Figure S1B,C, Supporting Information). Since the solid phase technique does not allow the recovery of non-imprinted nanoparticles, biotin-derivatized glass beads were also prepared in parallel to synthesize MINPs against an unrelated molecule, thus serving as negative controls (Figure S1A, Supporting Information). Figure 2C,D shows scanning transmission electron microscopy (STEM) images of MINPs synthesized against biotin (BINPs) and TGF-β3 epitope (TEINPs), respectively. Direct measurements in STEM images (Figure 2E) and dynamic light scattering (DLS) assays (Figure 2F; and Table S1, Supporting Information) both show an overlapping size distribution for the two types of MINPs, although BINPs present a slightly larger average diameter in either case (75 $\pm$ 21 vs 69 $\pm$ 22 nm by STEM, P = 0.0027; 196.5 $\pm$ 3.6 vs 179.0 $\pm$ 5.5 nm by DLS, P = 0.0017). Electrophoretic light scattering measurements (Table S1 and Figure S2, Supporting Information) show a negative Zeta potential for both types of MINPs, with TEINPs being slightly more negative than BINPs (−27.1 $\pm$ 0.9 mV vs −32.3 $\pm$ 3.1 mV, P = 0.0080). Despite the statistical significance of these differences, the average values for size and surface charge for both types of MINPs lie well within the same order of magnitude. Therefore, we considered that the imprinting process with different template molecules did not significantly alter the essential physicochemical properties of synthesized MINPs.

Next, we studied the interaction between MINPs and the target TGF-β3 conformational epitope by surface plasmon resonance (SPR) technique. Immobilization of MINPs on the SPR sensor chip surface could hide the imprinted cavity, thus hindering the rebinding of the epitope peptide. Therefore, we opted for immobilizing the peptide instead, by covalently coupling its exposed amine groups to the carboxyl groups of the carboxymethyl dextran layer of the sensor chip. Figure 2H,I display representative sensorgrams corresponding to five injections at increasing concentrations of BINPs and TEINPs, respectively. Figures S3 and S4 (Supporting Information) show these graphs in greater detail along with some of the relevant quality assessment parameters for the TEINP sensorgram. Additionally, they also show the components of the fitting curves after deconvolution, helping to separate specific binding phenomena (dark blue) from unspecific response derived from bulk and drift effects (light blue).

Due to the relatively large size of MINPs, both SPR sensorgrams show pronounced bulk effects, represented by a square wave-like signal. The serial increases in this component denote the increasing nanoparticle concentrations with each injection. It is also possible to observe that BINPs seem to generate a higher bulk response compared to TEINPs, despite the same molar concentration being used for both. Since BINPs present a slightly larger size, they should also have a correspondingly higher molar mass, thereby helping to explain this difference. By contrast, considering the specific binding component, the behaviors of the two types of MINPs are sharply distinct. BINPs demonstrated no specific interaction with the immobilized epitope, with a poor fit for the SPR measurements (Figure 2H; Figure S3B, Supporting Information). On the other hand, TEINPs generated typical association and dissociation curves describing a binding interaction with the immobilized epitope. These resulted in a good fit (Figure 2I; Figure S4A, Supporting Information) which allowed the calculation of an equilibrium dissociation constant, K_D = 18 $\pm$ 13 nM (Table S2, Supporting Information). A previous study analyzing antibody affinities in detail would place this value around the lower end of the affinity spectrum, with most antibodies presenting a K_D < 1 nM.[44] If we look at the binding kinetics, the association rate (k_{on}) for TEINPs falls precisely in the average order of magnitude calculated in this study (10^5 M^{-1} s^{-1}), while the dissociation rate (k_{off}) is two orders of magnitude higher

ADVANCED
SCIENCE NEWS

www.advancedsciencenews.com

ADVANCED
FUNCTIONAL
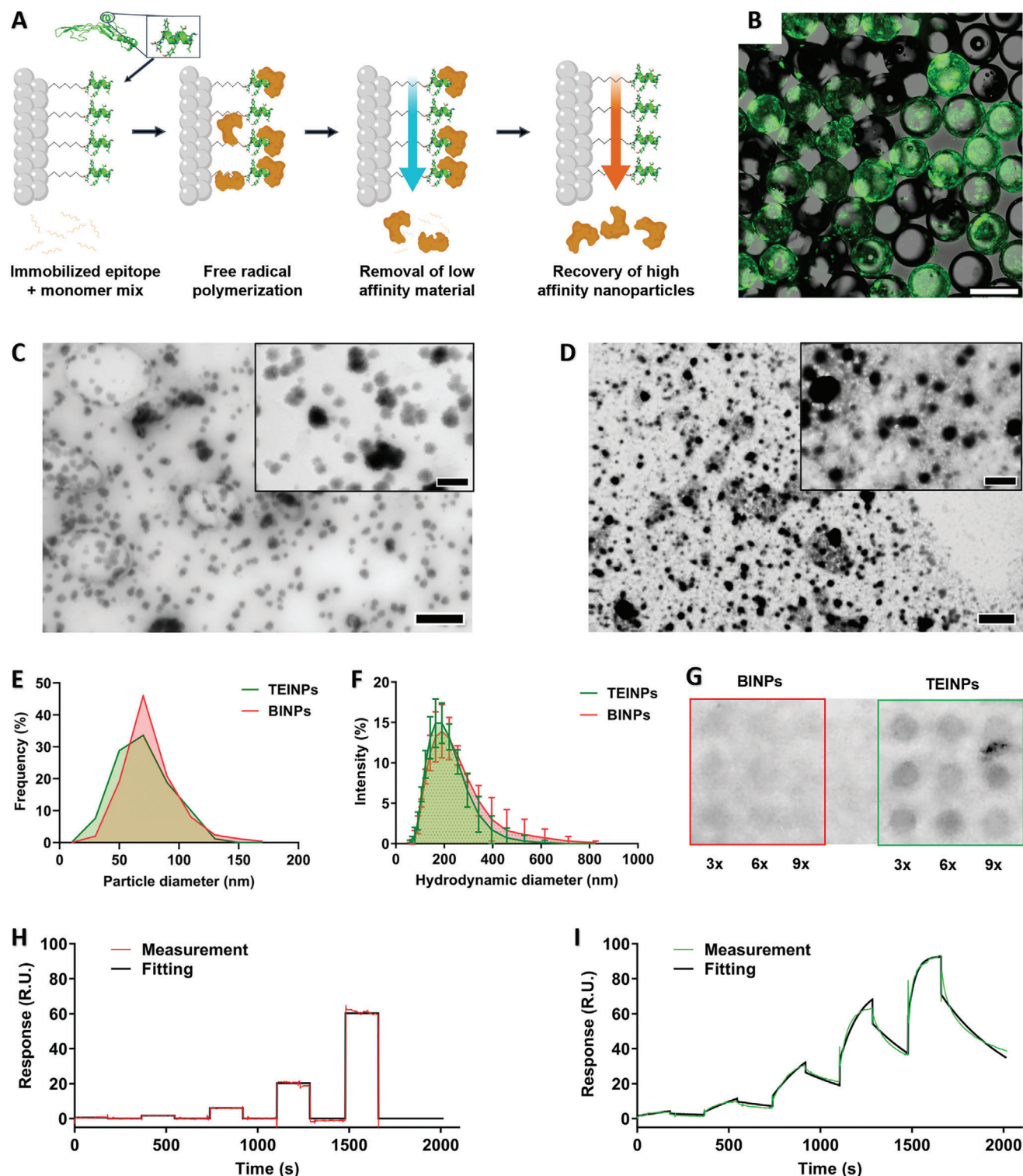**MATERIALS**

www.afm-journal.de

Figure 2. Production and characterization of molecularly imprinted nanoparticles (MINPs). A) Schematic of solid phase imprinting method. B) Confocal microscopy image of fluorescein-labeled epitope-functionalized glass beads. Green fluorescence image is superimposed on brightfield image. Scale bar: 100 μm. C,D) Scanning transmission electron microscopy (STEM) visualization of (C) biotin-imprinted MINPs (BINPs) and (D) TGF-β3 epitope-imprinted MINPs (TEINPs). Scale bars: 500 nm; inset scale bars: 200 nm. E) Histogram of MINP diameter distribution as measured in STEM images ($n = 250$). F) Histogram of MINP hydrodynamic diameter distribution measured by dynamic light scattering. Data presented as mean $\pm$ standard deviation (BINPs, $n = 3$; TEINPs, $n = 6$). G) Dot blot assessment of recombinant human TGF-β3 retained by MINPs after three, six, or nine cycles of precipitation and washing. H,I) Representative surface plasmon resonance sensorgrams (red/green) and corresponding fits (black) of (H) BINP and (I) TEINP interaction with immobilized TGF-β3 epitope.

**ADVANCED
SCIENCE NEWS**

www.advancedsciencenews.com

**ADVANCED
FUNCTIONAL
MATERIALS**

www.afm-journal.de

than the average found for antibodies (10^{-3} vs 10^{-5} s^{-1}). This implies that the interaction between MINPs and the target epitope is more unstable, being essentially limited by the dissociation step. Nonetheless, the K_D calculated in the present work compares quite favorably with typical values expected for epitope-imprinted polymers,[35] also falling within the range of most commercially available mouse monoclonal antibodies.[45,46]

Next, we assessed if this affinity behavior in TEINPs is translated to the full TGF-β3 protein. Because the immobilization of the protein on the SPR sensor chip could occur via the target epitope, therefore hampering the binding of injected MINPs, the interaction between MINPs and the target GF was evaluated in free form in a liquid environment.[31] MINPs were incubated with commercially available recombinant human (rh)TGF-β3, followed by several cycles of precipitation and washing. The remaining rhTGF-β3 adsorbed to the nanoparticles was then detected by a dot blot immunoassay. As shown in Figure 2G, BINPs retained very low amounts of protein after only three cycles, with no detectable level after nine cycles. Instead, TEINPs retained a relatively stable level of bound TGF-β3 even after nine washing cycles, demonstrating that the imprinting process was successful in generating a suitable affinity for the full target protein. Moreover, despite the previous considerations regarding dissociation rates and the stability of this interaction, TEINPs proved effective at retaining the GF, an essential feature for the proposed application.

2.2. Magnetically Responsive Microfibers can be Efficiently Aligned in Gelatin Hydrogels

The next step in our strategy requires the development of biomimetic microarchitectures within 3D constructs, thereby attaining adequate control over the biophysical environment at the cellular scale. Specifically, recreating the fibrillar uniaxial anisotropy of the tendon core ECM has been shown to be a key element for directing cellular behavior toward a tenocytic phenotype in different tissue engineered constructs.[47–49] Electrospinning-based scaffolds are among the most explored biomaterials due to the ability of this technique to generate micro-/nano-scaled fiber structures, which closely resemble the natural tendon ECM.[38,47,50] However, here we envisioned a system where cells can develop in a fully biomimetic 3D environment, instead of simply on the surface of the scaffold. Furthermore, this system should be sufficiently versatile to allow different forms of processing, such as direct injection for repairing small defects or 3D bioprinting of larger constructs.[51] We thus looked toward the post-processing of electrospun fiber meshes into short microfibers that can be incorporated within polymeric hydrogels to fabricate composites with improved properties.[20,52] These microfibers are a versatile microscale material, granting several levels of control over different properties, such as length and interfiber spacing. To allow these microfibers to introduce anisotropy into the system, magnetic nanoparticles can be incorporated into their production, endowing them with magnetic responsiveness. This enables their remote orientation within the hydrogel networks by applying non-invasive external magnetic fields, resulting in anisotropic composite fibrillar materials without requiring the direct application of other external mechanical forces.[53]

To achieve these goals, we followed our previously developed fabrication process,[20] which is schematically described in Figure S6A (Supporting Information). We started by synthesizing zinc-doped iron oxide magnetic nanoparticles (MagNPs) by a thermal decomposition route (Figure S5, Supporting Information). The incorporation of zinc cations in the structure of MagNPs has previously been demonstrated as an efficient design strategy to increase their magnetization values in comparison with non-doped iron oxide MagNPs.[54,55] In this way, our biomaterials can be provided with the desired magnetic response by incorporating lower amounts of MagNPs and remotely manipulated by applying weak magnetic fields, thus minimizing the toxicity/safety risks associated with these factors. The performed magnetometer measurements confirmed the large magnetization values of the designed zinc-doped MagNPs, up to 75.1 ± 3.1 emu g^{-1}, and their superparamagnetic behavior, essential to prevent their uncontrolled aggregation when external magnetic radiation is applied. (Figure S5E and Table S3, Supporting Information).

MagNPs were then included in a polycaprolactone (PCL) solution and electrospun into aligned fiber meshes using a device with a rotating drum collector. These were then sectioned in a microtome-cryostat and redispersed, obtaining sMRFs with an average length of 65 ± 21 µm (Figure S6D, Supporting Information, shows sMRF length distribution). The aligned electrospinning procedure likely contributed to reducing interfibrillar interactions and fiber entanglement, leading to an adequate dispersiveness of sMRFs after cryosectioning (Figure S6C, Supporting Information). The successful incorporation of MagNPs inside sMRFs was confirmed by transmission electron microscopy (TEM) (Figure S6E, Supporting Information). Moreover, magnetometry measurements showed that the designed sMRFs display magnetic responses proportional to the amount of incorporated magnetic material, while keeping the superparamagnetic behavior observed for pure MagNPs (Figure S6F,G and Table S4, Supporting Information).

Next, we evaluated the capability of the obtained sMRFs to be remotely aligned within gelatin-based hydrogels through the application of external low-intensity magnetic fields. For that, freeze-dried sMRFs were dispersed at different concentrations in gelatin solutions, with cross-linking being triggered by the addition of transglutaminase at physiological temperature. These mixtures were placed inside custom-made 3D printed holders (Figure S7A, Supporting Information), with three pairs of magnets producing a fairly uniform magnetostatic field of 13.9 ± 1.8 mT over each sample during gelation. As shown in **Figure 3A** and Figure S7B (Supporting Information), encapsulated sMRFs could be efficiently aligned within the gelatin hydrogels, remaining fixed in place after they are fully cross-linked. Moreover, we also verified that sMRF concentration of up to 3 g L^{-1} can be incorporated without relevant levels of aggregation using the current protocol. This is an important point to consider since aggregates might negatively affect the intended uniaxial anisotropy of tendon biomimetic constructs and, consequently, cell guidance responses. On the other hand, sMRF concentration must be sufficiently high in order to generate a densely packed fibrillar microstructure that can effectively influence cellular organization. If the interfibrillar distance becomes too large, the probability of cell contact guidance decreases drastically,
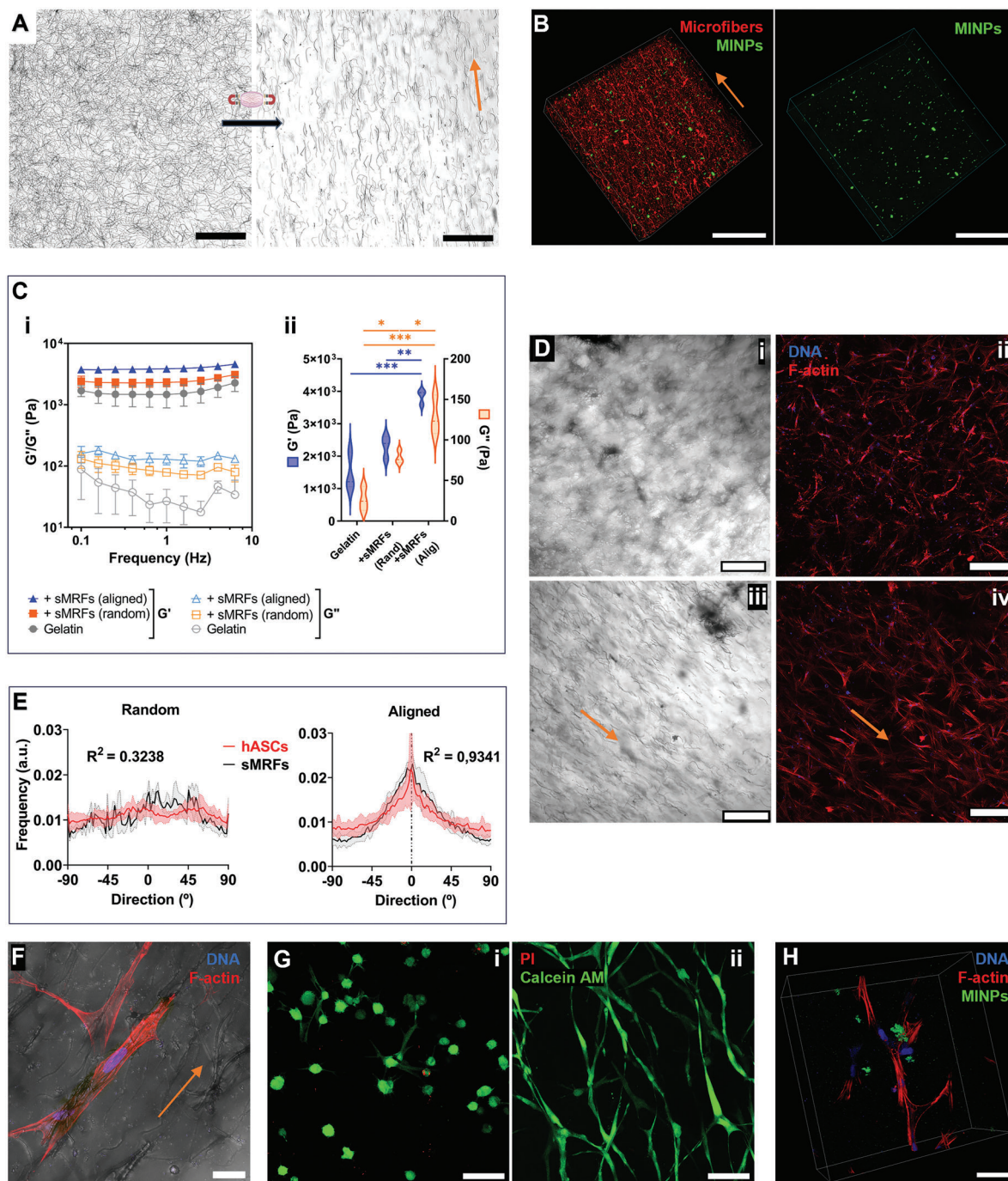
**ADVANCED
SCIENCE NEWS**

www.advancedsciencenews.com

**ADVANCED
FUNCTIONAL
MATERIALS**

www.afm-journal.de

Figure 3. Encapsulation of human adipose tissue-derived stem/stromal cells (hASCs) in hydrogels containing short magnetically responsive microfibers (sMRFs) and molecularly imprinted nanoparticles (MINPs). A) Optical microscopy images of sMRFs (3 g L^{-1}) in suspension (left) and after alignment and gelation (right). Scale bars: 200 µm. Orange arrows represent the direction of the magnetic field applied during gelation. B) Confocal microscopy 3D reconstructions of gelatin hydrogel with rhodamine-labeled sMRFs (red) and fluorescein-containing MINPs (green). Scale bars: 200 µm. C) (i) Shear storage (G') and loss (G") moduli versus angular frequency plots of neat gelatin hydrogels and gels with 3 g L^{-1} random or magnetically-aligned sMRFs. Data presented as mean ± standard deviation (SD) of three independent measurements. (ii) Statistical analysis performed for samples at 1 Hz frequency by one-way Analysis of Variance (ANOVA) followed by Tukey's post hoc tests (*$p < 0.05$; ** $p < 0.01$; *** $p < 0.001$). D) Confocal microscopy images of tenogenic constructs without (i, ii) or with (iii, iv) magnetic alignment of sMRFs. i,iii) brightfield images showing sMRFs. ii, iv) fluorescence images showing encapsulated hASCs. Red: F-actin; blue: DNA. Scale bars: 200 µm. E) Directionality histograms derived from confocal microscopy images; random: $n = 8$; aligned: $n = 12$; data presented as mean (bold line) ± SD (light filling). Correlation between sMRF and hASC orientation was assessed by calculating Pearson correlation coefficients ($p < 0.0001$). F) Confocal microscopy image of tenogenic construct showing hASCs adhering to aligned sMRFs. Red: F-actin; blue: DNA. Scale bar: 25 µm. G) Representative confocal microscopy images of calcein AM (green)/propidium iodide (PI; red) staining of hASCs within tenogenic constructs with aligned sMRFs and containing 1.5 g L^{-1} TGF-β3 epitope-MINPs. Scale bars: 100 µm. i) day 1; ii) day 7. H) Confocal microscopy 3D reconstruction of tenogenic construct showing distribution of MINPs around encapsulated hASCs. Red: F-actin; blue: DNA; green: MINPs. Scale bar: 50 µm.

**ADVANCED
SCIENCE NEWS**

www.advancedsciencenews.com

**ADVANCED
FUNCTIONAL
MATERIALS**

www.afm-journal.de

resulting in isotropic cell growth.[20] Henceforth, this concentration was chosen for subsequent experiments.

Afterwards, we evaluated the incorporation and spatial distribution of MINPs within the anisotropic hydrogels. To allow their visualization, fluorescently-labeled nanoparticles were prepared by including a fluorescent monomer (fluorescein *O*-methacrylate) during the polymerization step of MINP synthesis. Then, fluorescent MINPs were added to the gelatin/sMRF mixture before adding the cross-linking agent. Figure 3B shows confocal microscopy images of hydrogels with rhodamine-labeled sMRFs (red) along with fluorescein-containing MINPs (green). As can be seen in both images, MINPs tended to aggregate into small microscale clusters. This is probably due to the preparation method, which requires all components to be at 37 °C to maintain gelatin in a fluid state. The MINPs used in this work are thermoresponsive due to the inclusion of N-isopropylacrylamide in their composition, entering a collapsed hydrophobic state above ca. 32 °C. While this is necessary for their preparation by solid phase imprinting, it causes nanoparticle aggregation in aqueous media at physiological temperature. This is supported by DLS analysis of MINPs at different temperatures (Figure S8, Supporting Information) showing a significant, albeit reversible, increase in polydispersity and average size at 37 °C, with microscale particle aggregates appearing within a broad size distribution. Nonetheless, a significant number of relatively well-dispersed nanoparticles can be observed alongside these MINP clusters, with an even distribution throughout the hydrogels. Furthermore, despite several washing steps after gelation, these nanoparticles remained stably embedded into the hydrogel network, demonstrating the applicability of this formulation for the following studies with stem cells. A probable consequence of this lower colloidal stability is the inaccessibility of some MINP binding sites that can become hidden within particle aggregates. This can lead to a lower maximum TGF-β3 binding capacity compared to an ideal nanoparticle dispersion, with a corresponding lower global effect on stem cell signaling. Strategies to mitigate this undesired behavior should be therefore tested in future studies, for example, by using different MINP compositions or synthesis methods.

Then, to assess how sMRF incorporation impacts the mechanical properties of gelatin hydrogels, we conducted rheological tests on gels containing the selected concentration of sMRFs (Figure 3C). Results demonstrate that TG-cross-linked gelatin hydrogels behave as typical viscoelastic materials with predominant solid-like behavior and a relatively frequency-independent storage modulus (*G'* between 1 – 4 kPa) in the range of frequencies tested. As expected from previous works on similar fibrillar composite hydrogels, both from our own team and from other groups,[20,48,56] the incorporation of sMRFs has an overall reinforcing effect, increasing bulk hydrogel stiffness compared to neat gelatin. However, unlike previous systems, this reinforcement effect is higher in aligned samples, where *G'* is about three-fold higher than the gelatin base level (p < 0.001), and also higher compared to gels with randomly oriented sMRFs (p < 0.01). This unexpected outcome suggests that sMRF organization has an impact on the hydrogel network formation. A possible explanation for this effect might be related with the enzymatic gelling process used in this work. Unlike the very fast photocross-linking taking place, for example, when using methacrylated gelatin,[20] TG-

mediated cross-linking kinetics are far slower, taking over 30 min to reach the maximum cross-linking level of gelatin networks. During this process, it appears that sMRF organization somehow interferes with the hydrogel network formation, where the aligned samples with lower sMRF percolation seem to favor the cross-linking promoted by TG. Although the precise nature of the observed bulk hydrogel reinforcement by aligned sMRFs should be further elucidated, it positively contributes for the potential of these hydrogels in regenerative applications of mechanically demanding tissues like tendon.

2.3. Anisotropic Fibrous Hydrogels Influence Cellular Morphology and TGF-β Signaling Patterns

The developed anisotropic fibrous hydrogel was then used to assemble full tenogenic constructs by encapsulating human adipose tissue-derived stem/stromal cells (hASCs) along with MINPs and aligned sMRFs in gelatin hydrogels. hASCs were chosen for these experiments since they are a widely available and easily accessible type of mesenchymal stem cell.[57] These cells have wide-ranging plasticity, with the potential to differentiate into various musculoskeletal phenotypes, including the tenogenic lineage, depending on the stimulation provided.[58]

We started by culturing tenogenic constructs in standard culture conditions and observing cell development by confocal microscopy after fluorescent staining of their cytoskeleton. As shown in Figure 3D-ii,iv, encapsulated hASCs thrived within the hydrogels, showing a homogeneous distribution throughout the gel volume. Remarkably, cytoskeleton patterns closely followed the microfiber alignment (Figure 3D-i,iii), both presenting very similar directionality peaks and distribution (Figure 3E). Higher magnification images (Figure 3F) seem to confirm that cells preferentially adhere to the sMRFs, using them as physical guides in the hydrogel 3D space. Moreover, this phenomenon leads to hASCs acquiring an elongated morphology typical of tendon resident cells, which was the targeted effect. This is a critical point since cell shape is a strong mechanotransduction priming factor for stem cell tenogenic differentiation.[59–62] Indeed, the very maintenance of tenocyte homeostasis is greatly influenced by mechanical signals, particularly tension.[63] These cues are translated into biological responses through a complex network, involving direct cytoskeletal links between cell membrane integrins and the nuclear envelope, as well as ion channels like PIEZO1/2 and signaling pathways such as the Hippo pathway.[63,64] In fact, a recent study precisely described how the loss of cell tension quickly changes chromatin configuration, downplaying the action of Hippo-members YAP/TAZ, while YAP overexpression counterbalances this effect.[65] These data support the previous notion that providing encapsulated stem cells with a biomimetic physical cue is likely to be essential in guiding their path toward tenogenesis by modulating their gene expression patterns.[55–58] Importantly, the viability of encapsulated hASC was not negatively affected by sMRF and MINP contents within tenogenic constructs, as assessed by LIVE/DEAD staining at both early (day 1) and later (day 7) timepoints (Figure 3G), with viable cells representing over 94% of the total number of cells in all conditions (Figure S9, Supporting Information). In sum, it was possible to confirm that the constructs are effective at controlling the

biophysical environment at the cellular scale, contributing to direct cell shape and spatial organization.

Next, we analyzed the effects of this engineered microenvironment on the activation of TGF-β3 signaling pathways of encapsulated hASCs. As a first step, we re-evaluated the distribution of MINPs in hydrogels, now including cultured cells. Figure 3H shows constructs with fluorescently stained hASCs along with green fluorescent TEINPs, that appear to be in close proximity to the cells at multiple points. This likely indicates that they are able to adequately sequester endogenously secreted TGF-β3 and bring it into increased contact with cell receptors, which is essential for the intended application.[62,63] Then, to efficiently quantify multiple targets of the TGF-β signaling cascade, we performed a multiplex immunoassay quantification on hASC lysates after 7 days of culture. Constructs stimulated by supplementation with exogenous rhTGF-β3 were used as positive controls, as this is a well-know tenogenesis-inducing stimulus,[66,67] including in strategies where it has been combined with anisotropic scaffolds.[68] Additionally, gels with incorporated BINPs and randomly oriented sMRFs were used as negative controls. To prepare these constructs, the same protocol was followed but in the absence of the magnetic field during gelation, thereby generating an isotropic sMRF organization within the hydrogels.

TGF-β acts as a dimer, binding to TGF-β type II receptor (TGFβRII) which recruits and phosphorylates TGF-β type I receptor (TGFβRI). TGFβRI then recruits and phosphorylates SMAD family members 2 and 3 (Smad2/3). Phosphorylated Smad2/3 (pSmad2/3) thus binds Smad4, creating a complex that enters the nucleus and acts as a transcription factor regulating gene expression.[69,70] Besides this so-called canonical Smad pathway, TGF-β receptors are also capable of activating other pathways, such as those mediated by protein kinase B (Akt) or extracellular signal-regulated kinases 1 and 2 (ERK1/2), which are also involved in downstream gene expression regulation. Figure 4A depicts these complex webs in a simplified scheme, helping to visualize the role of the proteins analyzed in our study. Accompanying the scheme are the relative quantification results for the total protein levels of TGFβRII (B), as well as for phosphorylated Akt (Ser473) (C), ERK1/2 (Thr185/Tyr187) (D), Smad2 (Ser465/Ser467) (E), and Smad3 (Ser423/Ser425) (F). Quantification of total Smad4 was not successful, since results for all samples were at least an order of magnitude below the level of the internal negative control provided in the assay kit. Therefore, the respective results were not included in this panel (see Figure S10, Supporting Information). Similarly, pSmad2 in the various samples also falls beneath the level measured for the internal negative control, which does not allow to draw conclusions.

Instead, for the other analytes, it is possible to see a general trend of increases in their relative levels in samples with TEINPs compared to those with BINPs, in particular at the higher nanoparticle concentration of 2 g L^{-1}, suggesting that TEINPs can indeed bind TGF-β3 secreted locally by hASCs and boost its paracrine activity. Looking at the results for total TGFβRII, the combination of sMRF alignment with the presence of TEINPs was essential to increase this marker to a level statistically significantly higher than in other samples. Indeed, the response obtained in these constructs was comparable to the one observed in constructs with incorporated TEINPs which were stimulated with exogenous rhTGF-β3, the benchmark for this assay. Inter-

estingly, this exogenous stimulation was not effective in constructs with BINPs, once again suggesting that GF activity is more complex than initially assumed, being dependent on the microenvironment surrounding the cells.[30,32] Another interesting outcome was that the inclusion of TEINPs led to a higher level of TGFβRII compared to the use of BINPs in randomly oriented constructs. However, this effect was not statistically significant and was less pronounced than in aligned hydrogels, suggesting an existing synergy between the biochemical and biophysical stimuli that govern cellular responses. A remarkably similar outcome was observed for Akt phosphorylation. In this case, only aligned hydrogels with the highest concentration of TEINPs attained a significantly higher level of pAkt, comparable to rhTGF-β3 stimulation. The similarity in the behavior of the two proteins might imply that TGFβRII is mainly acting in these systems through phosphorylation of Akt.

ERK1/2 phosphorylation was significantly more pronounced than that observed for other analytes. For this kinase, none of the tested conditions were able to match the outcome of exogenous GF stimulation, which was again amplified in samples with TEINPs compared to those with BINPs, confirming the ability of MINPs to boost target GF signaling (full statistical analysis of pERK1/2 results in Table S5, Supporting Information). Moreover, unlike pAkt or TGFβRII, random sMRF orientation actually seems to promote ERK1/2 phosphorylation compared to aligned hydrogels at the highest MINP concentration. Although further studies are required to fully corroborate this hypothesis, this result could suggest that the same biochemical stimulus (TGF-β3) is triggering different downstream responses depending on the physical properties sensed by cells. Nevertheless, it is in agreement with the current understanding of the interactions between mechanotransduction and GF signaling processes. For example, the geometry and spatial patterns of cell substrate topography have been shown to impact ligand clustering and interaction between GF receptors and integrins, thereby influencing cellular responses.[25] Lastly, although the alignment/TEINP combination also slightly increased Smad3 phosphorylation, no statistically significant differences were registered for this marker. Along with results for pSmad2 and total Smad4, the outcome of this assay implies that in these tenogenic constructs, the canonical Smad pathway is likely not the most relevant downstream effector of TGF-β signaling. Instead, there is a close association between TGFβRII and non-canonical Akt levels, which could explain the Smad results since Akt prevents phosphorylation of Smad3 and dampens activation of the Smad pathway.[22,69] Moreover, these results offer an interesting prospect for a multifactored manipulation of tissue engineered constructs, where the change of a single design parameter of the bioengineered microenvironment can program different cellular responses.

2.4. Encapsulated hASCs Significantly Shift Gene Expression and Protein Synthesis toward Tenogenesis

After confirming that hASCs adapt their responses to both the biophysical and biochemical elements integrated in tenogenic constructs, we next evaluated how this translates into their downstream phenotypic commitment. For this purpose, we analyzed by quantitative real-time polymerase chain reaction (qPCR) a
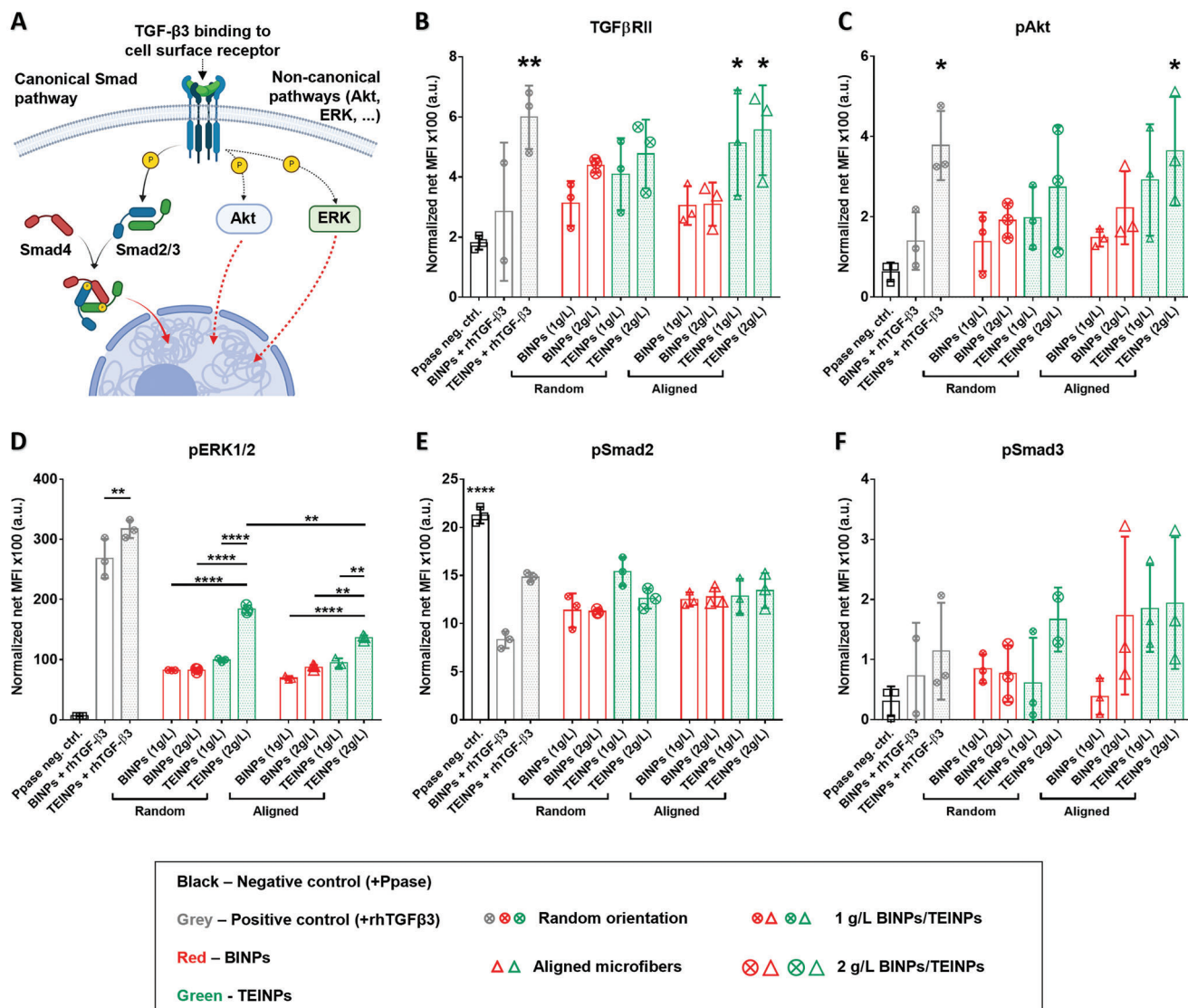
Figure 4. Multiplex immunoassay quantification of proteins in the transforming growth factor (TGF)-β signaling pathway after 7 days of culture. A) Schematic representing the different pathways analyzed. B) Quantification of TGF-β Receptor II (TGF-βRII), responsible for interacting with extracellular TGF-β3 and activating intracellular signaling cascades. C) Quantification of phosphorylated (p)Akt (protein kinase B), a serine/threonine-specific protein kinase that participates in multiple cellular processes. D) Quantification of pERK1/2 (phosphorylated extracellular signal-regulated kinases 1/2); when activated, pERK1/2 translocate to the nucleus to phosphorylate intranuclear targets involved in processes like proliferation or differentiation. E,F) Quantification of pSmad2/3, two receptor-regulated Smads involved in direct signaling from TGF-β receptors. When phosphorylated, they form a trimer with the common partner Smad (Smad4), entering the nucleus to regulate DNA transcription. Net median fluorescence intensity (MFI) values for each analyte were normalized to those of glyceraldehyde 3-phosphate dehydrogenase (GAPDH) and are presented as 100-fold to facilitate reading. +Ppase – protein phosphatase treatment; +rhTGF-β3 – recombinant human TGF-β3 supplementation (2 ng mL^{-1}, 1 h); BINPs – biotin-imprinted nanoparticles; TEINPs – TGF-β3 epitope-imprinted nanoparticles. Data presented as mean $\pm$ standard deviation ($n = 3$). Statistical analysis by one-way Analysis of Variance (ANOVA) followed by Tukey's post hoc tests (* $p < 0.05$, ** $p < 0.01$, **** $p < 0.0001$). Full statistical analysis results for pERK1/2 available in Table S5 (Supporting Information), along with results for Smad4 (Figure S10, Supporting Information).

panel of gene expression markers associated with tenogenesis and tendon repair[71] in hASCs cultured for 14 days (**Figure 5A**). Results are displayed as fold changes relative to gene expression in gels with randomly oriented sMRFs and with no MINPs, defined as the reference condition for this assay. Each gene was analyzed across a range of five concentrations of TEINPs, in constructs with either randomly oriented (empty circles) or magnetically aligned (full squares) sMRFs.

Looking at the results in Figure 5A, it is possible to clearly distinguish two patterns of gene expression, depending on the orientation of microfibers. Except for *COL1A1*, for which no significant differences were found (**Table 1**), all other gene markers show different expression trends according to each biophysical setting where cells were cultured. In general, a positive correlation is observed between the expression of all five markers and the concentration of TEINPs in aligned constructs,
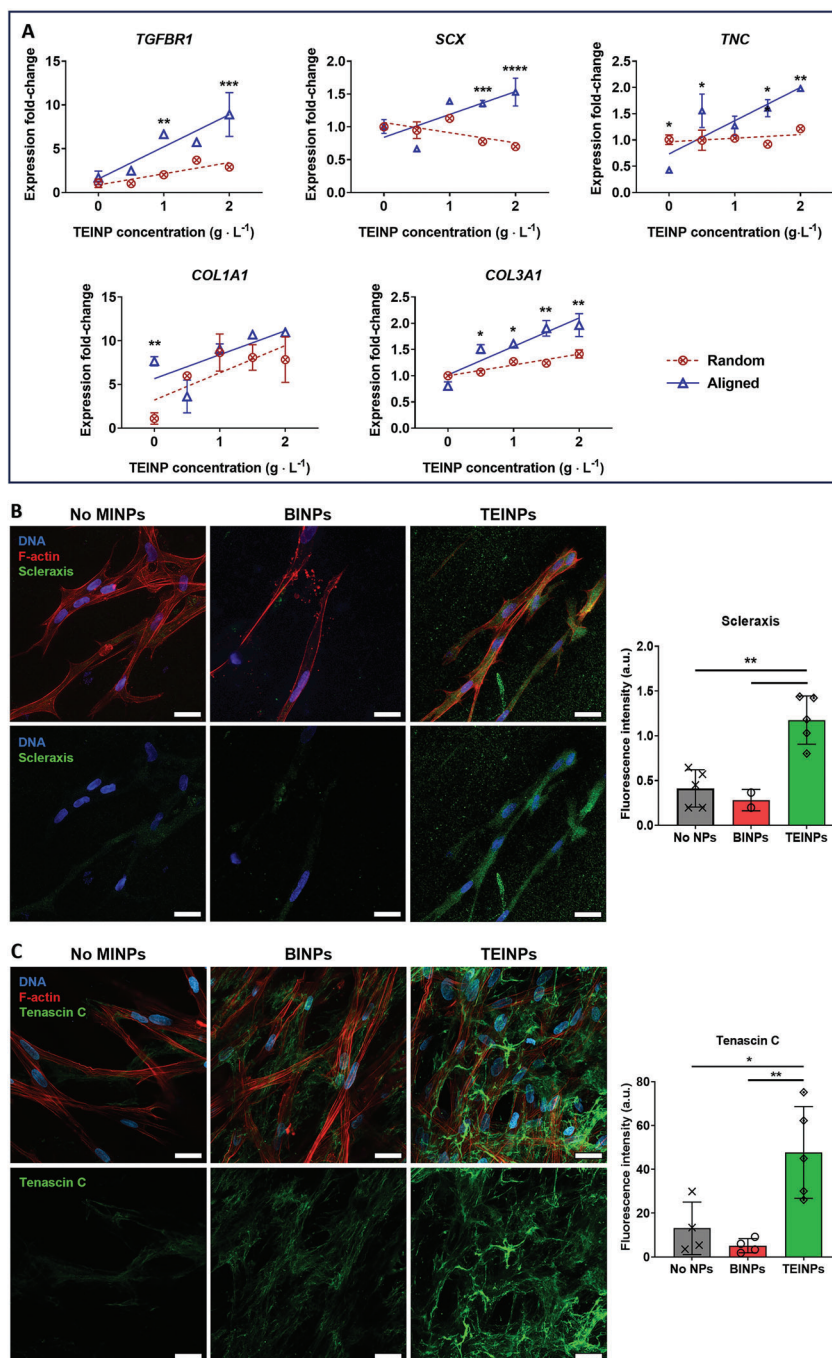
**ADVANCED
SCIENCE NEWS**

www.advancedsciencenews.com

**ADVANCED
FUNCTIONAL
MATERIALS**

www.afm-journal.de

Figure 5. Biological response of human adipose tissue-derived stem/stromal cells (hASCs) encapsulated in tenogenic constructs. A) Quantitative real-time polymerase chain reaction (qPCR) results for gene markers associated with tenogenesis: *TGFBR1* – transforming growth factor beta receptor 1; *SCX* – scleraxis bHLH transcription factor; *TNC* – tenascin C; *COL1A1* – collagen type I alpha 1 chain; *COL3A1* – collagen type III alpha 1 chain. Results are normalized to transcript levels of *YWHAZ* and displayed as fold changes relative to gene expression in gels with randomly oriented short magnetically responsive microfibers (sMRFs) and with no molecularly imprinted nanoparticles ($n = 2$). Statistical analysis by two-way Analysis of Variance (ANOVA) followed by Šidák's post hoc tests. Stars represent significant differences at the same concentration between hydrogels with aligned (blue triangles) and randomly oriented (red circles) sMRFs (* $p < 0.05$, ** $p < 0.01$, *** $p < 0.001$, **** $p < 0.0001$). Curves represent linear regressions of gene expression levels as a function of TGF-β3 epitope-imprinted nanoparticle (TEINP) concentration in hydrogels (further details in Table 1). B) Immunocytochemistry images of hASCs encapsulated in anisotropic constructs (scale bars: 25 μm; red: F-actin; blue: DNA; green: scleraxis) and respective quantification of scleraxis transcription factor (no NPs, TEINPs, $n = 5$; BINPs, $n = 2$). Green fluorescence levels were normalized to red fluorescence values in each image. Statistical analysis by one-way ANOVA followed by Tukey's post hoc tests (** $p < 0.01$). C) Immunocytochemistry images of encapsulated hASCs (scale bars: 25 μm; red: F-actin; blue: DNA; green: tenascin C) and corresponding quantification for glycoprotein tenascin C (no NPs, BINPs, $n = 4$; TEINPs, $n = 5$). Green fluorescence levels were normalized against the number of nuclei present in each image. Statistical analysis by one-way ANOVA followed by Tukey's post hoc tests (* $p < 0.05$, ** $p < 0.01$). All quantitative data are presented as mean ± standard deviation.

**ADVANCED
SCIENCE NEWS**

www.advancedsciencenews.com

**ADVANCED
FUNCTIONAL
MATERIALS**

www.afm-journal.de

Table 1. Select parameters of linear regressions of gene expression levels as a function of TGF-β3 epitope-imprinted nanoparticle concentration in tenogenic constructs.

Gene marker	Random R^2	Aligned R^2	P value[a]
TGFBR1	0.7175	0.8156	0.0360 (*)
SCX	0.4644	0.5797	0.0007 (***)
TNC	0.1671	0.6902	0.0028 (**)
COL1A1	0.5363	0.4960	0.7928 (ns)
COL3A1	0.8908	0.8184	0.0038 (**)

[a] P values are respective to calculated slopes for aligned versus randomly oriented hydrogels ($n = 2$). Slope pairs with P values below 0.05 are considered significantly different (* $p < 0.05$, ** $p < 0.01$, *** $p < 0.001$). TGFBR1 – transforming growth factor beta receptor 1; SCX – scleraxis bHLH transcription factor; TNC – tenascin C; COL1A1 – collagen type I alpha 1 chain; COL3A1 – collagen type III alpha 1 chain.

consistent with a directing of stem cell fate commitment toward tenogenesis. In contrast, the expression pattern of analyzed gene markers in randomly oriented constructs behaves quite differently. For instance, TGFBR1 (encoding TGF-β receptor 1) is upregulated by TEINPs in both types of gels, but at significantly higher levels in the aligned ones–2.9 versus 8.9-fold-change at 2 g L^{-1} MINPs (P = 0.0005). This outcome is in good agreement with the results previously observed for TGFβRII quantification in the multiplex immunoassay, indicating that TEINPs are likely promoting a positive feedback loop of TGF-β signaling that is amplified by microstructural alignment. A similar effect was observed for COL3A1 (collagen type III alpha 1 chain), with expression levels increasing 2.0-fold in aligned constructs versus 1.4-fold in random ones (P = 0.0023). Collagen type III is the second most abundant collagen in tendon ECM and is essential for the correct fibrillogenesis of collagen type I, its main component.[72–74] On the other hand, COL1A1 is significantly upregulated by the alignment of sMRFs when no MINPs are present (7.7-fold, P = 0.0034). Interestingly, the inclusion of TEINPs attenuates this difference, raising the expression of COL1A1 to comparable levels in both construct types, although with a slight advantage for aligned hydrogels (7.8 to 8.7-fold in random, 9.1 to 11-fold in aligned, P > 0.1).

An interesting finding can be seen for the gene expression of scleraxis transcription factor (SCX), which is among the most specific tendon- and ligament-associated markers. It works as a master switch for tendon lineage specification during development, as well as for tendon healing after injury,[75] being known to be activated by TGF-β signaling.[3,76] The performed qPCR analysis shows a higher expression of SCX with increasing TEINP concentrations (1.5-fold at 2 g L^{-1}), but this effect only occurs in aligned constructs. In contrast, in isotropic gels, SCX is downregulated by TEINPs (0.7-fold at the highest concentration). These opposing trends suggest that the same biochemical stimulus (TGF-β) generates different cellular responses depending on the physical microenvironment. These results are well aligned with the TGF-β pathway activation findings discussed above, showing that different signaling pathways are being activated according to the anisotropy degree of the system. A comparable behavior can be seen for TNC, corresponding to the glycoprotein tenascin C which is prevalent in tendon ECM.[72,77] While its expression remains virtually unchanged along the TEINP concen-

tration axis in random orientation gels, there is a clear upregulation trend caused by the increasing presence of TEINP within constructs with aligned sMRFs. (2.0-fold versus 1.2-fold at 2 g L^{-1} MINPs, P = 0.0018). Together, these results may indicate that, in an isotropic setting, the increased TGF-β stimulation is guiding hASCs down a different differentiation pathway other than the tenogenic lineage. In a previous work, we have demonstrated that TEINPs promote the chondrogenic phenotype in hASCs when cultured in scaffold-free cell pellets.[31] A similar effect might be happening in these composites with randomly-oriented sMRFs, although analysis of additional gene and protein targets would be required to confirm this hypothesis.

Finally, to verify if this behavior extended beyond gene expression to protein synthesis, we performed immunocytochemistry staining experiments for SCX and TNC. Representative images and their corresponding quantifications are shown in Figure 5B (SCX) and C (TNC), comparing anisotropic constructs with either no MINPs, 1.5 g L^{-1} BINPs, or 1.5 g L^{-1} TEINPs (moderately-high concentration based on previous assays). The outcomes for both proteins were not only remarkably similar between the two, but also supported previous qPCR findings. No significant differences could be detected in the SCX expression levels of hASCs cultured in BINP-based hydrogels compared to those with no MINPs. On the other hand, the use of TEINPs significantly boosted its detection levels by a factor of 2.9 – 4.2 (P < 0.01). Likewise, de novo deposition of TNC in the pericellular matrix of hASCs was fairly low in hydrogels either without any MINPs or with BINPs, but significantly higher in cultures with TEINPs. Normalized fluorescence intensity associated with TNC was 3.7 times higher in gels with TEINPs compared to no MINPs (P = 0.0156) and 9.3 times higher compared to gels with BINPs (P = 0.0043). Overall, these protein detection results closely match the preceding gene expression findings, corroborating our main hypothesis.

Taken together, these results strongly suggest that hASC fate commitment is being synergistically driven toward a tenogenic phenotype by a combination of i) TGF-β signaling modulation via MINP binding with ii) contact guidance of cell shape and organization by the hydrogel anisotropic fibrous architecture. Not only is it apparent that the gene expression signature of hASCs is shaped in tandem by these factors, but protein synthesis also shifts in a similar manner, confirming a pronounced change in cell behavior. These findings support the proposed hypothesis, opening new possible biomaterials driven strategies toward tendon regeneration therapies. A particularly interesting direction to explore would be by implementing this concept using sMRFs modified with tendon dECM, as we have recently proposed,[20] to better recreate the biochemical cues of tendon niche and thus provide hASCs multiple signals that synergistically contribute to boost their tenogenesis.

Importantly, the basic principles of this biomaterial design concept can be easily readapted for the engineering of other tissues. Although additional studies will be needed to unequivocally demonstrate the hypothesis, our data regarding the various cell responses seem to indicate that changing a single parameter – like microfiber orientation – might be sufficient to drastically change stem cell commitment using the same platform. In fact, it has been recently shown that isotropic fibrous microstructures within collagen-based hydrogels act as inducers of mesenchymal

**ADVANCED
SCIENCE NEWS**

www.advancedsciencenews.com

**ADVANCED
FUNCTIONAL
MATERIALS**

www.afm-journal.de

stem cell chondrogenesis.[78] Our composite hydrogels have the potential to be an improvement over this type of system since they allow independent tuning of the hydrogel topography without complex fabrication techniques. In addition, the magnetic responsiveness of sMRFs could be leveraged after gelation to deliver contactless magneto-mechanical stimulus to encapsulated cells,[20] increasing the level of control over bioengineered tissue dynamics to guide encapsulated stem cell fate.[73]

In future developments, it would be interesting to evolve the present system considering specific requirements of the cell niche. For example, tissue development and healing are dynamic processes that require variable inputs at different stages.[79] Moreover, full scale tendons have a well-defined hierarchical structure, with spatially distinct physical and biological characteristics.[1] Thus, (photo)patterning the proposed constructs with different mechanical properties and tissue-specific biofunctionalities or exploring the proposed composite hydrogels as bioinks for 3D bioprinting platforms would allow an additional degree of spatiotemporal control over microenvironmental cues.[80–82] It is worth mentioning that several recent studies have cleverly used aptamers as GF affinity ligands that can release the bound molecules on demand by the introduction of their complementary sequences.[83,84] However, the need for external molecular triggers to induce the release of sequestered molecules poses additional implementation difficulties in therapeutical settings. Thus, designing innovative materials with programmable responses to endogenous stimuli such as cell traction forces seems a more attractive route.[85] Nevertheless, all these concepts have focused on the controlled binding and release of exogenous GFs. The use of synthetic MINPs as sequestering elements that amplify endogenous paracrine signaling is a significant competitive advantage of our system. In this context, the design of MINPs with controlled biodegradability[86,87] might be an attractive option to obtain materials with additional cell responsive properties. Importantly, a comparative edge of epitope imprinting for the synthesis of GF sequestering motifs is that the template can be rationally selected from the surface of target molecules while avoiding regions in their topology recognized by the corresponding receptor, thus avoiding masking their biological effects until their release is triggered.[30,35] Although this functional challenge of molecular recognition would be possible to address with other biological protein binders, abiotic MINPs have a flexibility and speed of design at costs that cannot be matched by those alternatives.

3. Conclusion

In this work, we have designed a composite hydrogel system that can provide simultaneous control over both physical and biochemical stimuli synergistically contributing for guiding the response of encapsulated stem cells toward tenogenic commitment. On the one hand, we have shown that the use of completely synthetic molecularly imprinted nanoparticles as tailor made GF sequestering units is an effective alternative for replacement, or at least a significant reduction of exogenous stimulation with recombinant GFs. This single finding holds the potential to drastically reduce the costs and widen the accessibility of tissue engineering approaches. On the other hand, short magnetically-responsive electrospun microfibers can be

used to generate microstructural anisotropy that mimics the architecture and topography of tendon ECM within the hydrogels, leading to ordered stem cell organization by microcontact guidance mechanisms. To combine both tools, a simple but effective gelatin-based hydrogel system was used, constituting an adequate biomimetic environment to support stem cell survival and growth. In general, the strategy presented here leverages several functional components to collectively control different cues in 3D bioengineered microenvironments, thus precisely controlling stem cell fate in tissue engineered constructs. Lastly, it is important to note that each component of this study was conceived following the principles of cost-effectiveness and scalability, which are essential for future clinical translation. Importantly, the concepts explored here can also be easily adapted to meet the specific needs of different tissues in future TERM developments. In conclusion, this work not only culminates the development of several biomaterial tools intended for tendon regeneration therapies, but it also opens the perspective for new advances in the field built on the present design concepts.

4. Experimental Section

Solid Phase Imprinting of MINPs – Glass Bead Derivatization with Template Molecule: Protocol adapted from Ref.[43] First, glass bead surface was activated by boiling in 1 M NaOH (PanReac AppliChem, Spain, 0.8 mL of solution per gram of glass beads) for 15 min, and then thoroughly rinsing with deionized water (eight times with 3.33 mL g^{-1} beads). PBS was used to neutralize the base (5 mL g^{-1} beads) followed by repeated rinsing with deionized water to remove potential salt residues (until pH was ca. 7). Beads were rinsed twice with acetone (3.33 mL g^{-1} beads) and dried at 80 °C for 3 h. Afterward, incubated the dry beads in a freshly prepared solution of either (3-aminopropyl)trimethoxysilane or (3-glycidyloxypropyl)trimethoxysilane 2% (v/v) in anhydrous toluene (Carlo Erba, France) for 24 h at room temperature (RT) (0.4 mL g^{-1} beads). Beads were not stirred but simply swirled gently by hand from time to time, as collisions between beads abrade the surface and lead to the formation of glass dust. Then, they were decanted onto a sintered disc filter funnel, rinsed with at least eight volumes of acetone and one volume of methanol, and left to dry under vacuum. For biotin immobilization, amine-functionalized beads were incubated overnight in PBS pH 7.4 (0.4 mL g^{-1} beads) containing 0.5 g L^{-1} biotin, 10 g L^{-1} N-(3-dimethylaminopropyl)-N′-ethylcarbodiimide hydrochloride (EDC), and 15 g L^{-1} N-hydroxysuccinimide (NHS).For TGF-β3 conformational epitope immobilization, epoxy-functionalized beads were incubated overnight in 10 mM carbonate buffer pH 9.0 (1 mL g^{-1} beads) containing 0.2 g L^{-1} epitope (CNCKAPTALCTNYCFRN, cysteine bridges C$_1$–C$_{11}$ and C$_3$–C$_{15}$, GeneCust, France). The resulting epitope-beads were then washed several times with carbonate buffer (8 × 8 mL g^{-1} beads). Unreacted epoxide groups were blocked with 1 M ethanolamine pH 9.0 (3 mL g^{-1} beads) for 2 h followed by washing with PBS (8 × 8 mL g^{-1} beads). Finally, beads were rinsed with deionized water (15 × 8 mL g^{-1} beads) on a sintered disc filter funnel, under vacuum. For confirmation of functionalization, biotin-beads were incubated with 0.5% (v/v) streptavidin, Alexa Fluor 488 conjugates (Thermo Fisher, USA) in PBS, for 1 h at RT, followed by rinsing 3 times with deionized water. Epitope-beads were incubated in 0.05% (w/v) FITC in carbonate buffer pH 9.3 for 3 h at 37.5 °C, followed by rinsing 3 times with the same buffer. Fluorescently labelled beads were then observed in a Leica TCS SP8confocal microscope.

Solid Phase Imprinting of MINPs – Polymerization: N-isopropylacrylamide (3.4 mM), N,N′-methylenebisacrylamide (0.13 mM), N-*tert*-butylacrylamide (2.6 mM), acrylic acid (0.32 mM), and N-(3-aminopropyl)methacrylamide hydrochloride (0.33 mM) were dissolved in ultrapure (UP) water. To produce fluorescent MINPs for microscopy

ADVANCED
SCIENCE NEWS

www.advancedsciencenews.com

ADVANCED
FUNCTIONAL
MATERIALS

www.afm-journal.de

visualization, fluorescein *O*-methacrylate (0.065 mM) was added to the previous solution. The solution was degassed by sonicating under vacuum using a Sonics VCX-130PB-220 with 13 mm probe for 15 min. followed by purging with N_2 for 30 min via a long needle. Template-derivatized glass beads were degassed by performing three cycles of alternate vacuum/N_2. The degassed solution of monomers was poured onto the glass beads while swirling gently by hand and flushing the flask with N_2 for 5–10 min. Next, ammonium persulfate (0.26 M) and tetramethylethylenediamine (0.66 M) in UP water were added through a long needle into the bulk of the mixture while swirling gently to homogenize. Reacted for 2 h at room temperature (RT) under N_2 flow, periodically swirling it gently by hand. After synthesis, the mixture was transferred to a solid phase extraction tube fitted with a 20-μm porosity polyethylene frit. The tube was fitted to a filtering flask and the solution was removed by vacuum and replaced with fresh deionized water at RT. Unreacted monomers and low-affinity polymers were removed by eluting this solution at RT and by replacing it with 30-mL aliquots of fresh deionized water for 9 times. Then, the outlet of the tube was closed, 30 mL of fresh deionized water (prewarmed at 70 °C) were added to the glass beads, and the tube was placed in a water bath at 70 °C for 15 min. After incubation, MINPs were collected by applying vacuum. The previous incubation was repeated 3 times for 2 min. each. The collected MINP suspension was concentrated by ultrafiltration using Amicon Ultra-15 Centrifugal Filter Units (30 kDa molecular weight cutoff), performing consecutive centrifugations at 15 °C for 5 min. at 3200 × g, until the final desired volume. The resulting suspension was then freeze-dried, and the yield was calculated by weighing the dry nanoparticles.

Determination of MINP Affinity and Selectivity for Template Epitope by SPR: Biacore X100 (Cytiva, Sweden) was used throughout the following procedures. All solutions were filtered through a 0.22 μm filter before being used with Biacore X100. Sensor chip CM5 (Cytiva, Sweden) was used to immobilize TGF-β3 conformational epitope. First, scouted the best pH to maximize ligand immobilization. TGF-β3 conformational epitope was diluted to 0.5 mg mL^{-1} in 10 mM acetate buffer at pH 4.5, 5.0, and 5.5. Followed Biacore Wizard Template for pH scouting procedure in flow cell no. 2 (Fc2), using PBS-P+ buffer 1x (Cytiva, Sweden) as running buffer. Regeneration buffer was composed of 50 mM sodium hydroxide and 1 M sodium chloride in UP water. Since maximal response was achieved at pH 5.0, proceeded with the immobilization of TGF-β3 epitope on Fc2 using Biacore Wizard template parameters: i) flow rate: 5 μL min^{-1}, ii) contact time: 360 s, iii) target immobilization level: 5000 RU (response units), iv) ligand: 500 μg mL^{-1} TGF-β3 conformational epitope in pH 5.0 acetate buffer. Blank immobilization was performed on the reference Fc1, by loading it with a mixture of EDC (75 g L^{-1}; Cytiva) and NHS (11.5 g L^{-1}; Cytiva), followed by ethanolamine HCl pH 8.5 (1.0 M, Cytiva) to block reactive groups. Final response level (Fc2 – Fc1) was 3823.3 RU. Finally, regeneration buffer was injected 5 times for 30 s onto the chip surface to remove loosely bound molecules.

To assess MINP interaction with the template epitope, Biacore single cycle kinetics standard procedure was followed, consisting in five successive injections at increasing concentrations onto the sensor chip. Apparent MINP molarities (*[MINPs]*, mol L^{-1}) were calculated according to Equation 1,[88]

$$[MINPs] = \frac{6}{\pi N_A d^3 \rho} X \tag{1}$$

where N_A is Avogadro's number (mol^{-1}), d is the hydrodynamic diameter of particles (cm), ρ is the polymer density (g cm^{-3}), and X is polymer weight concentration (g L^{-1}). The ρ values for *N*-isopropylacrylamide-based swollen particles were estimated by Ogawa et al. to be ≈0.01 g cm^{-3}.[89] A start-up cycle was performed to stabilize the sensor chip surface, where running buffer (PBS-P+ 1x) was injected 5 consecutive times. Two blank cycles were then performed using the same settings as the assay proper, but injecting running buffer instead of MINP samples. Finally, MINPs were injected at increasing concentrations for 90 s each, with 300 s of dissociation time after the last injection. A single injection of regeneration buffer for 60 s was performed to clean the

sensor surface at the end of the run. The resulting sensorgram was analyzed using Biacore X100 Evaluation Software™. Reference curves (Fc1) were automatically subtracted from each active sensorgram. The average of the two blank cycles was then also subtracted from the test run sensorgram. The subtracted curves were finally fit using 1:1 binding kinetics model. Three replicates were performed for BINPs, while 6 replicates were performed for TEINPs.

Characterization of MINP Affinity for Target TGF-β3 Protein by Dot Blot: To assess the affinity of MINPs for the full target protein, these were incubated at 37 °C for 1 h in a solution of 1 g L^{-1} rhTGF-β3 (PeproTech, Thermo Fisher, USA) in PBS. Afterward, MINPs were precipitated by centrifuging at 12 300 × g for 15 min. The supernatant was removed and MINPs were washed with fresh PBS by vortexing for 10 s. This precipitation/washing procedure was repeated for a total of either 3, 6, or 9 times. Then, supernatant from the last cycle was removed, MINPs were resuspended in 1x Laemmli's Loading Buffer and heated to 95 °C for 5 min in an Eppendorf Thermomixer to denature and release the protein. Five microliters of solution were pipetted in triplicate onto a nitrocellulose membrane which was left to dry overnight. The membrane was blocked for 1 h at RT with a solution of 1% (w/v) bovine serum albumin (BSA) and 5% (w/v) milk powder (Nestlé Molico, Portugal) in Tris-buffered saline with Tween 20 (TBST), followed by an overnight incubation with anti-human TGF-β3 rabbit antibody (ab15537, Abcam, UK) (0.173 μg mL^{-1} in blocking buffer).After rinsing with TBST, the membrane was incubated for 1 h at RT with IRDye 800CW anti-Rabbit IgG secondary antibody (LI-COR Biosciences, USA) (0.1 μg mL^{-1} in TBST). Finally, it was rinsed 3 times with TBST, followed by water, and the results visualized in an Odyssey Fc Imaging System.

Fabrication of Short Magnetically-Responsive Microfibers (sMRFs): Poly-ϵ-caprolactone (PCL) was dissolved at 17% (w/v) in 70:30 chloroform/dimethylformamide, and MagNPs[55] were added at 5% (w/w) (relative to polymer weight); 0.1% (w/w) rhodamine was also added in some batches to visualize microfibers in fluorescence microscopy. The solution was left stirring overnight to homogenize. Two electrospinning setups were tested. First, a vertically oriented system, with a static target, was used to prepare randomly spun meshes, spinning for 30 min. per fiber mesh. Next, a HolmarcHO-NFES-043 model electro-spinning unit with a rotating drum target was used to prepare aligned meshes, spinning for 45 min per mesh. The following settings were used in both systems: i) needle-to-target $d = 12.5$ cm, ii) $\Delta V = 13.1$ kV, iii) flow (Φ) = 1 mL h^{-1}, and iv) syringe diameter $d = 12.25$ mm.

Meshes were left to dry overnight to ensure complete evaporation of solvents. Dry meshes were cut into small rectangular pieces (*ca*. 1 cm sides), which were immersed in optimal cutting temperature (OCT) compound (Thermo Scientific) (*ca*. 1 cm high) inside a cylindrical tin foil container. The mixture was frozen with liquid nitrogen vapors and stored at −20 °C overnight to form a solid block. Blocks were then cut in a Cryostat Microm HM550 into slices with a set thickness of 50 μm. Slices were immersed in a warm water bath (40 °C) to melt OCT and release the sMRFs. These were precipitated using a magnet and the supernatant discarded and replaced with warm deionized water, followed by vigorous stirring to rinse the sMRFs. This was repeated 3–5 times, until no more foam from OCT was observed. To redisperse sMRF aggregates, they were manually divided into smaller pieces with a tweezer and placed in 1.5-mL tubes with 0.5 mL UP water. Then, each aliquot was repeatedly passed through the following materials in succession, until aggregates no longer decreased in size and clogged the structure: 1000 μL micropipette tip, 200 μL micropipette tip, 18, 21, and 25 G needles. The recovered suspensions were strained through a tea infuser to remove remaining aggregates, frozen at −80 °C, and lyophilized for 72 h.

Human Adipose Tissue-Derived Stem Cell (hASC) Culture: Human liposuction aspirates were obtained from healthy female anonymous donors under informed consent and according to protocols approved by the Ethical Committee of Hospital da Prelada (Porto, Portugal, Approval No. 005/2019). hASCs were isolated from lipoaspirates according to a standard protocol with collagenase digestion. Cells were plated in complete Alpha-Modified Eagle's Minimum Essential Medium and incubated in a humidified atmosphere at 37 °C with 5% CO_2. Culture

**ADVANCED
SCIENCE NEWS**

www.advancedsciencenews.com

**ADVANCED
FUNCTIONAL
MATERIALS**

www.afm-journal.de

medium was replaced every 3 days and cells were subcultured at 80% confluence.

Preparation of Tenogenic Constructs: Transglutaminase (TG) enzyme (ACTIVA WM, Ajinomoto Foods Europe, France) was dissolved in PBS (200 g L^{-1}) and placed at 37 °C, 4–5 h before starting the experiment to activate the enzyme. Gelatin (type A from porcine skin) was dissolved at 5% (w/v) in PBS for 1 h at 70 °C, followed by 3–4 h at 37 °C. sM-RFs were suspended (3 g L^{-1}) in gelatin solution by up-and-down pipetting (G-MF mixture). TG solution, G-MF mixture, and MINPs were UV-sterilized for 30 min before being used with hASCs. Cells were trypsinized and resuspended (10^6 mL^{-1}) in G-MF mixture, to which TG was then added (12.5 µL per mL of cell suspension, corresponding to 5 units of active enzyme per gram of gelatin). Next, MINPs were resuspended in this mixture at 0; 0.5; 1; 1.5; or 2 g L^{-1}, thoroughly mixing by up-and-down pipetting. Ten microliters of each sample were transferred in triplicate to 15-well Ibidi µ-Slide Angiogenesis and left in a cell culture incubator for 30 min to ensure gelation. To prepare aligned constructs, µ-slides were placed during this step inside a custom-made holder (Figure S7A, Supporting Information), with 3 pairs of magnets producing a relatively uniform magnetic field over the samples. After gelation, 50 µL of culture medium were added to each well and changed every 2 days for the length of culture.

Analysis of TGF-β Pathway Activation by Multiplex Immunoassay: MIL-LIPLEX Human TGFβ Signaling 6-plex Magnetic Bead Kit (48-614MAG) was used on day 7 of culture according to manufacturer's instructions. GAPDH (glyceraldehyde 3-phosphate dehydrogenase) MAPmate (46-667MAG) was used simultaneously to serve as reference for normalization of other protein levels. To prepare positive controls, tenogenic constructs were stimulated directly with rhTGF-β3 (PeproTech, USA). Selected constructs were serum-starved for 4 h, followed by addition of rhTGF-β3 for 1 h (final concentration 2 ng mL^{-1}). Immediately after stimulation, proceeded with cell lysis as follows. Culture medium was removed, and gels washed with ice cold PBS. Gels were retrieved from culture slides with a spatula and placed in 1.5-mL centrifuge tubes with ice-cold 1x MILLIPLEX Lysis Buffer with freshly added protease inhibitors. Samples were homogenized using a Tissue Grinder Mixy Professional, followed by repeatedly passing through 18 and 21 G needles. After gently rocking for 10 min at 4 °C, particulate matter was removed by ultrafiltration using Ultrafree-MC, DV 0.65 µm-pore centrifugal filter units, spinning at 12 000 × g for 4 min at 4 °C. The filtered liquid fraction was stored at -80 °C until further processing. For the immunoassay, all samples and reagents were prepared according to manufacturer instructions and the kit protocol was precisely followed. The plate was read using a Luminex MAGPIX instrument. Relative protein levels were calculated using the instrument software, by subtracting background fluorescence levels (given by Assay Buffer) and dividing by the corresponding GAPDH levels for normalization. All results were multiplied by 100 to facilitate reading.

RNA Extraction and Gene Expression Analysis by qPCR: To analyze gene expression, constructs were carefully retrieved with a spatula, placed in TRI Reagent (0.5 mL per 3 gels) and stored at −80 °C for at least 24 h. Samples were homogenized using a Tissue Grinder Mixy Professional, followed by repeatedly passing through 21 and 25 G needles (at least 15 times each). Afterward, total RNA was extracted following manufacturer's protocol. RNA concentration and purity were assessed using a NanoDrop ND-1000 spectrophotometer. Five hundred twenty five nanograms of total RNA were reversely transcribed using qScript cDNA Synthesis Kit (Quanta Biosciences, USA). qPCR was performed using PerfeCTA SYBR Green FastMix (Quanta Biosciences, USA), according to the manufacturer's protocol, and run on Mastercycler ep Realplex Thermocycler. Primer sequences (Table S6, Supporting Information) were designed using Primer-BLAST NCBI tool and synthesized by Eurofins Genomics (Luxemburg).

Melting curves were analyzed at the end of every reaction to verify specificity of PCR products. 2$^{-\Delta\Delta Ct}$ method was used to calculate relative gene expression.[90] *YWHAZ* was chosen as reference gene marker, due to the stability of its expression across the sample sets. All values were first normalized to average transcript levels of *YWHAZ*, and then to gene expres-

sion in cells seeded in randomly oriented gels without MINPs (control group), as given by Equation 2:

$$R = 2^{-[\Delta Ct\,sample - \Delta Ct\,control]} \tag{2}$$

being R the relative expression ratio of each gene of interest (GOI), ΔCt sample the difference between the crossing points (Ct) of GOI and the average of reference genes in each sample, and ΔCt control the difference between the Ct of GOI and the average of reference genes in control group.

Cell Morphology Observation and Immunocytochemistry Staining: To evaluate the presence of selected proteins, immunocytochemical analysis was performed after 14 days of culture. Cells were fixed with 10% (v/v) neutral buffered formalin (Thermo Fisher Scientific, USA), washed with PBS and permeabilized with 0.1% (v/v in PBS)Triton X-100. Samples were then blocked with 1% (w/v in PBS) BSA for 1 h at RT, followed by incubation with primary antibody diluted in blocking buffer, either against scleraxis (ab58655, Abcam, UK, 1.25 µg mL^{-1}) or tenascin-C (MA1-26779, Thermo Fisher, USA, 2.0 µg mL^{-1}) overnight at 4 °C. Cells were subsequently washed with PBS, incubated with the corresponding Alexa Fluor 488-conjugated secondary antibody [for scleraxis, donkey anti-rabbit (A21206, Life Technologies, USA); for tenascin-C, donkey anti-mouse (A21202, Thermo Fisher, USA)] at the manufacturer's recommended dilution for 1 h at RT and counterstained with 4′,6-diamidino-2-phenylindole (1 µg mL^{-1} in PBS) and phalloidin–tetramethylrhodamine B isothiocyanate (0.5 µg mL^{-1} in PBS). Immunolabeled samples were visualized either in a Leica TCS SP8 or in a Zeiss LSM 980 confocal laser scanning microscope.

Statistical Analysis: All statistical analyses were performed using GraphPad Prism 9.5.1 software. All quantitative data in Figures 2F, 3, 4, and 5 are presented as mean ± standard deviation. The histogram in Figure 2E was derived from pooling all available measurements from STEM/TEM images into a single data group. SPR kinetic curves in Figure 2H,I are representative sensorgrams for each type of MINP. G' and G'' at 1 Hz frequency in Figure 3C-ii were analyzed by one-way Analysis of Variance (ANOVA) followed by Tukey's post hoc tests. Histograms in Figure 3E were calculated using the Directionality Analysis v2.3.0 function in ImageJ software, using the Fourier components method. sMRF and hASC orientation were compared by calculating Pearson's Correlation coefficients, with two-sided calculation of P value. Figure 4 multiplex results: Net median fluorescence intensity (MFI) data processing was described in its own subsection. Statistical analysis was conducted by one-way ANOVA followed by Tukey's post hoc tests. Figure 5A qPCR results: Expression level calculation was described in its own subsection. Statistical analysis for each marker was performed by two-way ANOVA followed by Šidák's post hoc tests. Gene expression levels versus TEINP concentration were fit with a simple linear regression, with the goodness of fit given by R^2, and slopes being tested for significant differences between "random" and "aligned" groups. Figure 5B,C immunofluorescence quantification: ImageJ software was used to determine the green fluorescence level, which was normalized against the number of nuclei present in each image. Statistical analysis was performed by one-way ANOVA followed by Tukey's post hoc tests. Alpha value threshold was set to α = 0.05 for all analyses where applicable. Sample size for each analysis and significance symbol meanings are provided in the respective Figure captions.

Supporting Information

Supporting Information is available from the Wiley Online Library or from the author.

Acknowledgements

Conflict of Interest

The authors declare no conflict of interest.

Data Availability Statement

The data that support the findings of this study are available from the corresponding author upon reasonable request.

Keywords

[1] J. G. Snedeker, J. Foolen, *Acta Biomater.* **2017**, *63*, 18.
[2] S. Ruiz-Alonso, M. Lafuente-Merchan, J. Ciriza, L. Saenz-del-Burgo, J. L. Pedraz, *J. Controlled Release* **2021**, *333*, 448.
[3] R. Aicale, N. Maffulli, F. Oliva, in *Human Orthopaedic Biomechanics*, Elsevier, Amsterdam **2022**, pp. 485–499.
[4] Y. Xu, H. Yin, J. Chu, D. Eglin, T. Serra, D. Docheva, *Biomater. Sci.* **2021**, *9*, 1237.
[5] M. Gomez-Florit, C. J. Labrador-Rached, R. M. A. Domingues, M. E. Gomes, *Adv. Drug Delivery Rev.* **2022**, *185*, 114299.
[6] C. Lee, *Orthop Trauma* **2021**, *35*, 274.
[7] Y. J. No, M. Castilho, Y. Ramaswamy, H. Zreiqat, *Adv. Mater.* **2020**, *32*, 1904511.
[8] G. Walden, X. Liao, S. Donell, M. J. Raxworthy, G. P. Riley, A. Saeed, *Tissue Eng. Part B Rev.* **2017**, *23*, 44.
[9] J. Petzold, E. Gentleman, *Front. Cell Dev. Biol.* **2021**, *9*, 3112.
[10] C. J. Bettinger, R. Langer, J. T. Borenstein, *Angew. Chem., Int. Ed.* **2009**, *48*, 5406.
[11] C. F. Guimarães, A. P. Marques, R. L. Reis, *Adv. Mater.* **2022**, *34*, 2105645.
[12] K. Zhou, B. Feng, W. Wang, Y. Jiang, W. Zhang, G. Zhou, T. Jiang, Y. Cao, W. Liu, *Int. J. Nanomed.* **2018**, *13*, 3867.
[13] J. Huang, Y. Chen, C. Tang, Y. Fei, H. Wu, D. Ruan, M. E. Paul, X. Chen, Z. Yin, B. C. Heng, W. Chen, W. Shen, *Cell. Mol. Life Sci.* **2019**, *76*, 505.
[14] V. Kishore, W. Bullock, X. Sun, W. S. van Dyke, O. Akkus, *Biomaterials* **2012**, *33*, 2137.
[15] A. Z. Unal, J. L. West, *Bioconjugate Chem.* **2020**, *31*, 2253.
[16] J. Xing, N. Liu, N. Xu, W. Chen, D. Xing, *Adv. Funct. Mater.* **2022**, *32*, 2110676.
[17] M. Hua, S. Wu, Y. Ma, Y. Zhao, Z. Chen, I. Frenkel, J. Strzalka, H. Zhou, X. Zhu, X. He, *Nature* **2021**, *590*, 594.
[18] M. Chau, S. E. Sriskandha, D. Pichugin, H. Thérien-Aubin, D. Nykypanchuk, G. Chauve, M. Méthot, J. Bouchard, O. Gang, E. Kumacheva, *Biomacromolecules* **2015**, *16*, 2455.
[19] M. T. I. Mredha, Y. Z. Guo, T. Nonoyama, T. Nakajima, T. Kurokawa, J. P. Gong, *Adv. Mater.* **2018**, *30*, 1704937.
[20] A. Pardo, S. M. Bakht, M. Gomez-Florit, R. Rial, R. F. Monteiro, S. P. B. Teixeira, P. Taboada, R. L. Reis, R. M. A. Domingues, M. E. Gomes, *Adv. Funct. Mater.* **2022**, *32*, 2208940.
[21] A. Pardo, M. Gómez-Florit, S. Barbosa, P. Taboada, R. M. A. Domingues, M. E. Gomes, *ACS Nano* **2021**, *15*, 175.
[22] P. C. D. P. Dingal, R. G. Wells, D. E. Discher, *Proc. Natl. Acad. Sci. USA* **2014**, *111*, 18104.
[23] A. Halim, A. D. Ariyanti, Q. Luo, G. Song, *Stem Cell Rev. Rep.* **2020**, *16*, 661.
[24] W. Y. Tong, W. Shen, C. W. F. Yeung, Y. Zhao, S. H. Cheng, P. K. Chu, D. Chan, G. C. F. Chan, K. M. C. Cheung, K. W. K. Yeung, Y. W. Lam, *Biomaterials* **2012**, *33*, 7686.
[25] A. Cipitria, M. Salmeron-Sanchez, *Adv. Healthcare Mater.* **2017**, *6*, 1700052.
[26] W. Man, S. Yang, Z. Cao, J. Lu, X. Kong, X. Sun, L. Zhao, Y. Guo, S. Yao, G. Wang, X. Wang, *Biomaterials* **2021**, *276*, 120971.
[27] J. Li, Y. Liu, Y. Zhang, B. Yao, Enhejirigala, Z. Li, W. Song, Y. Wang, X. Duan, X. Yuan, X. Fu, S. Huang, *Front. Cell. Dev. Biol.* **2021**, *9*, 640388.
[28] W. Cheng, Z. Ding, X. Zheng, Q. Lu, X. Kong, X. Zhou, G. Lu, D. L. Kaplan, *Biomater. Sci.* **2020**, *8*, 2537.
[29] W. Kim, H. Lee, J. Lee, A. Atala, J. J. Yoo, S. J. Lee, G. H. Kim, *Biomaterials* **2020**, *230*, 119632.
[30] S. P. B. Teixeira, R. M. A. Domingues, M. Shevchuk, M. E. Gomes, N. A. Peppas, R. L. Reis, *Adv. Funct. Mater.* **2020**, *30*, 1909011.
[31] S. P. B. Teixeira, R. M. A. Domingues, P. S. Babo, D. Berdecka, M. S. Miranda, M. E. Gomes, N. A. Peppas, R. L. Reis, *Adv. Funct. Mater.* **2021**, *31*, 2003934.
[32] D. G. Belair, N. N. Le, W. L. Murphy, *Chem. Commun.* **2014**, *50*, 15651.
[33] J. Crispim, H. A. M. Fernandes, S. C. Fu, Y. W. Lee, P. Jonkheijm, D. B. F. Saris, *Acta Biomater.* **2017**, *53*, 165.
[34] M. Gionet-Gonzales, A. Casella, D. Diloretto, C. Ginnell, K. H. Griffin, A. Bigot, J. K. Leach, *Adv. Healthcare Mater.* **2021**, *10*, 2101048.
[35] S. P. B. Teixeira, R. L. Reis, N. A. Peppas, M. E. Gomes, R. M. A. Domingues, *Sci. Adv.* **2021**, *7*, 9884.
[36] A. Poma, A. Guerreiro, S. Caygill, E. Moczko, S. Piletsky, *RSC Adv.* **2014**, *4*, 4203.
[37] A. Poma, A. Guerreiro, M. J. Whitcombe, E. v. Piletska, A. P. F. Turner, S. A. Piletsky, *Adv. Funct. Mater.* **2013**, *23*, 2821.
[38] M. Leung, S. Jana, C. T. Tsao, M. Zhang, *J. Mater. Chem. B* **2013**, *1*, 6516.
[39] C. Perucca Orfei, M. Viganò, J. R. Pearson, A. Colombini, P. De Luca, E. Ragni, L. Santos-Ruiz, L. De Girolamo, *Int. J. Mol. Sci.* **2019**, *20*, 149.

[40] A. I. Gonçalves, P. M. Gershovich, M. T. Rodrigues, R. L. Reis, M. E. Gomes, *J. Tissue Eng. Regener. Med.* **2018**, *12*, 762.

[41] K. Lyu, T. Liu, Y. Chen, J. Lu, L. Jiang, X. Liu, X. Liu, Y. Li, S. Li, *Eur. J. Med. Res.* **2022**, *27*, 75.

[42] J. Xu, P. X. Medina-Rangel, K. Haupt, B. Tse Sum Bui, In *NanoArmoring of Enzymes: Rational Design of Polymer-Wrapped Enzymes*, Academic Press, Cambridge, Massachusetts **2017**, pp. 115–141.

[43] F. Canfarotta, A. Poma, A. Guerreiro, S. Piletsky, *Nat. Protoc.* **2016**, *11*, 443.

[44] J. P. Landry, Y. Ke, G. L. Yu, X. D. Zhu, *J. Immunol. Methods* **2015**, *417*, 86.

[45] Y. Pan, E. K. Sackmann, K. Wypisniak, M. Hornsby, S. S. Datwani, A. E. Herr, *Sci. Rep.* **2016**, *6*, 39774.

[46] J. P. Landry, Y. Fei, X. Zhu, *Assay Drug Dev. Technol.* **2012**, *10*, 250.

[47] M. Laranjeira, R. M. A. Domingues, R. Costa-Almeida, R. L. Reis, M. E. Gomes, *Small* **2017**, *13*, 1700689.

[48] S. Araújo-Custódio, M. Gomez-Florit, A. R. Tomás, B. B. Mendes, P. S. Babo, S. M. Mithieux, A. Weiss, R. M. A. Domingues, R. L. Reis, M. E. Gomes, *ACS Biomater. Sci. Eng.* **2019**, *5*, 1392.

[49] A. Padhi, A. S. Nain, *Ann. Biomed. Eng.* **2020**, *48*, 1071.

[50] I. Calejo, C. J. Labrador-Rached, M. Gomez-Florit, D. Docheva, R. L. Reis, R. M. A. Domingues, M. E. Gomes, *Adv. Healthcare Mater.* **2022**, *11*, 2102863.

[51] S. M. Bakht, A. Pardo, M. Gómez-Florit, R. L. Reis, R. M. A. Domingues, M. E. Gomes, *J. Mater. Chem. B* **2021**, *9*, 5025.

[52] S. Poveda-Reyes, L. R. Mellera-Oglialoro, R. Martínez-Haya, T. C. Gamboa-Martínez, J. L. Gōmez Ribelles, G. G. Ferrer, *Macromol. Mater. Eng.* **2015**, *300*, 977.

[53] O. Kriha, M. Becker, M. Lehmann, D. Kriha, J. Krieglstein, M. Yosef, S. Schlecht, R. B. Wehrspohn, J. H. Wendorff, A. Greiner, *Adv. Mater.* **2007**, *19*, 2483.

[54] A. Pardo, S. Yáñez, Y. Piñeiro, R. Iglesias-Rey, A. Al-Modlej, S. Barbosa, J. Rivas, P. Taboada, *ACS Appl. Mater. Interfaces* **2020**, *12*, 9017.

[55] A. Pardo, B. Pelaz, J. Gallo, M. Bañobre-López, W. J. Parak, S. Barbosa, P. del Pino, P. Taboada, *Chem. Mater.* **2020**, *32*, 2220.

[56] A. Omidinia-Anarkoli, S. Boesveld, U. Tuvshindorj, J. C. Rose, T. Haraszti, L. De Laporte, *Small* **2017**, *13*, 1702207.

[57] P. Palumbo, F. Lombardi, G. Siragusa, M. Cifone, B. Cinque, M. Giuliani, *Int. J. Mol. Sci.* **2018**, *19*, 1897.

[58] A. I. Gonçalves, D. Berdecka, M. T. Rodrigues, A. D. Eren, J. Boer, R. L. Reis, M. E. Gomes, *J. Tissue Eng. Regener. Med.* **2019**, *13*, 2204.

[59] R. McBeath, D. M. Pirone, C. M. Nelson, K. Bhadriraju, C. S. Chen, *Dev. Cell* **2004**, *6*, 483.

[60] K. Kulangara, K. W. Leong, *Soft Matter* **2009**, *5*, 4072.

[61] A. R. Tomás, A. I. Gonçalves, E. Paz, P. Freitas, R. M. A. Domingues, M. E. Gomes, *Nanoscale* **2019**, *11*, 18255.

[62] Z. Yin, X. Chen, H. Song, J. Hu, Q. Tang, T. Zhu, W. Shen, J. Chen, H. Liu, B. C. Heng, H.-W. Ouyang, *Biomaterials* **2015**, *44*, 173.

[63] M. Lavagnino, M. E. Wall, D. Little, A. J. Banes, F. Guilak, S. P. Arnoczky, *J. Orthop. Res.* **2015**, *33*, 813.

[64] N. Felsenthal, E. Zelzer, *Development* **2017**, *144*, 4271.

[65] D. L. Jones, G. F. Hallström, X. Jiang, R. C. Locke, M. K. Evans, E. D. Bonnevie, A. Srikumar, T. P. Leahy, M. P. Nijsure, J. D. Boerckel, R. L. Mauck, N. A. Dyment, *Proc. Natl. Acad. Sci. USA* **2023**, *120*, 2211947120.

[66] Z. Kapacee, C.-Y. C. Yeung, Y. Lu, D. Crabtree, D. F. Holmes, K. E. Kadler, *Matrix Biol.* **2010**, *29*, 668.

[67] T. Barsby, D. Guest, *Tissue Eng. Part A* **2013**, *19*, 2156.

[68] M. Leung, S. Jana, C.-T. Tsao, M. Zhang, *J. Mater. Chem. B* **2013**, *1*, 6516.

[69] K. Tzavlaki, A. Moustakas, *Biomolecules* **2020**, *10*, 487.

[70] J. Massagué, *Nat. Rev. Mol. Cell Biol.* **2012**, *13*, 616.

[71] G. Nourissat, F. Berenbaum, D. Duprez, *Nat. Rev. Rheumatol.* **2015**, *11*, 223.

[72] N. L. Millar, K. G. Silbernagel, K. Thorborg, P. D. Kirwan, L. M. Galatz, G. D. Abrams, G. A. C. Murrell, I. B. McInnes, S. A. Rodeo, *Nat. Rev. Dis. Primers* **2021**, *7*, 1.

[73] H. Kuivaniemi, G. Tromp, *Gene* **2019**, *707*, 151.

[74] H. R. C. Screen, D. E. Berk, K. E. Kadler, F. Ramirez, M. F. Young, *J. Orthop. Res.* **2015**, *33*, 793.

[75] T. Sakabe, K. Sakai, T. Maeda, A. Sunaga, N. Furuta, R. Schweitzer, T. Sasaki, T. Sakai, *J. Biol. Chem.* **2018**, *293*, 5766.

[76] T. Barsby, D. Guest, *Tissue Eng. Part A* **2013**, *19*, 2156.

[77] F. Wu, M. Nerlich, D. Docheva, *EFORT Open Rev.* **2017**, *2*, 332.

[78] J. Yang, Y. Li, Y. Liu, D. Li, L. Zhang, Q. Wang, Y. Xiao, X. Zhang, *Acta Biomater.* **2019**, *91*, 159.

[79] P. He, D. Ruan, Z. Huang, C. Wang, Y. Xu, H. Cai, H. Liu, Y. Fei, B. C. Heng, W. Chen, W. Shen, *Front. Cell Dev. Biol.* **2022**, *10*, 821667.

[80] T. E. Brown, K. S. Anseth, *Chem. Soc. Rev.* **2017**, *46*, 6532.

[81] G. A. Primo, A. Mata, *Adv. Funct. Mater.* **2021**, *31*, 2009574.

[82] F. Huang, M. Chen, Z. Zhou, R. Duan, F. Xia, I. Willner, *Nat. Commun.* **2021**, *12*, 2364.

[83] D. Rana, P. Padmanaban, M. Becker, F. Stein, J. Leijten, B. Koopman, J. Rouwkema, *Mater. Today Bio* **2023**, *19*, 100551.

[84] D. Rana, A. Kandar, N. Salehi-Nik, I. Inci, B. Koopman, J. Rouwkema, *Bioact. Mater.* **2022**, *12*, 71.

[85] A. Stejskalová, N. Oliva, F. J. England, B. D. Almquist, *Adv. Mater.* **2019**, *31*, 1806380.

[86] Y.-T. Qin, Y.-S. Feng, Y.-J. Ma, X.-W. He, W.-Y. Li, Y. Zhang, *ACS Appl. Mater. Interfaces* **2020**, *12*, 24585.

[87] M. Gagliardi, A. Bertero, A. Bifone, *Sci. Rep.* **2017**, *7*, 40046.

[88] Y. Hoshino, T. Kodama, Y. Okahata, K. J. Shea, *J. Am. Chem. Soc.* **2008**, *130*, 15242.

[89] K. Ogawa, A. Nakayama, E. Kokufuta, *Langmuir* **2003**, *19*, 3178.

[90] K. J. Livak, T. D. Schmittgen, *Methods* **2001**, *25*, 402.